PLANETARY SCIENCE

Ground penetrating radar observations of subsurface structures in the floor of Jezero crater, Mars

Svein-Erik Hamran[1]*, David A. Paige[2], Abigail Allwood[3], Hans E. F. Amundsen[4], Tor Berger[1], Sverre Brovoll[1], Lynn Carter[5], Titus M. Casademont[1], Leif Damsgård[1], Henning Dypvik[1], Sigurd Eide[1], Alberto G. Fairén[6,7], Rebecca Ghent[8], Jack Kohler[9], Michael T. Mellon[7], Daniel C. Nunes[3], Dirk Plettemeier[10], Patrick Russell[2], Matt Siegler[8], Mats Jørgen Øyan[1]

The Radar Imager for Mars Subsurface Experiment instrument has conducted the first rover-mounted ground-penetrating radar survey of the Martian subsurface. A continuous radar image acquired over the Perseverance rover's initial ~3-kilometer traverse reveals electromagnetic properties and bedrock stratigraphy of the Jezero crater floor to depths of ~15 meters below the surface. The radar image reveals the presence of ubiquitous strongly reflecting layered sequences that dip downward at angles of up to 15 degrees from horizontal in directions normal to the curvilinear boundary of and away from the exposed section of the Séitah formation. The observed slopes, thicknesses, and internal morphology of the inclined stratigraphic sections can be interpreted either as magmatic layering formed in a differentiated igneous body or as sedimentary layering commonly formed in aqueous environments on Earth. The discovery of buried structures on the Jezero crater floor is potentially compatible with a history of igneous activity and a history of multiple aqueous episodes.

INTRODUCTION

Identifying and characterizing Martian lithological structures is a key goal for the Perseverance rover mission toward determining the geological history of Jezero crater and the geologic context of collected samples. Orbital imaging data have identified the presence of deltaic sedimentary structures deposited along the northern and western margins of the crater (*1*–*3*), but the nature and history of the Jezero crater stratigraphic sequence based on orbital observations has not been established conclusively (*4*–*6*). The Mars 2020 mission provides an opportunity to observe this sequence in situ (*7*, *8*). On Earth, ground-penetrating radar has become an invaluable tool for imaging otherwise inaccessible subsurface morphologies (*9*, *10*). The Radar Imager for Mars Subsurface Experiment (RIMFAX) ground-penetrating radar instrument on the Perseverance rover provides analogous subsurface imaging capabilities for Mars at spatial scales of tens of centimeter to hundreds of meters (*11*).

RESULTS

RIMFAX acquired a continuous radar image of the subsurface beneath the rover along traverses totaling ~2.6 km, starting at the landing location on 18 February 2021 (Sol 0) and ending on 19 September 2021 (Sol 204; Fig. 1) (*12*). The rover path generally curves around the Séitah structural feature on the Jezero crater floor and then heads eastward crossing the Artuby Ridge on Sol 201 and entering the Séitah formation. Figure 2 shows a three times vertically exaggerated, low-resolution radar image along the traverse path as a function of linear odometry, starting at Sol 86 and ending at Sol 204. After Sol 204, the rover then traversed ~160 m eastward within the Séitah formation to acquire samples at Brac and then traversed back westward toward the Artuby Ridge along a similar path to acquire samples at Issole. Figure 3 shows the rover path and low-resolution radar image of the Brac-Issole traverse.

RIMFAX imaging depths are calculated by assuming a spatially uniform, depth-independent radar propagation velocity of 0.1 m/ns, which is derived from fitting the shapes of 65 diffraction hyperbolas observed between Sols 47 and 210 using a geometric model that accounts for the height of the RIMFAX radar antenna above the surface (see Materials and Methods and fig. S1). The derived average velocity corresponds to a relative dielectric permittivity of 9.0, which is consistent with that expected for low-porosity rocks with mafic composition (see Materials and Methods) (*13*–*15*). Penetration depths vary spatially but are typically 15 m below the surface.

The RIMFAX radar images reveal the presence of ubiquitous subsurface layering along the rover's path (Figs. 2 and 3). Ground-penetrating radar layer reflections are caused by the presence of vertical contrasts in the dielectric properties on <10-cm scales. In the absence of interstitial liquid water, which is not expected to be present because of low Martian temperatures, reflectors can be attributed primarily to changes in the density/porosity of the subsurface (*16*, *17*). During Sols 113 to 127, 178 to 201, and 278 to 280, RIMFAX detects a thick near-surface layer that exhibits lower than average internal radar reflectivity. These low reflectivity zones indicate a relative absence of contrasting dielectric materials and of internal scattering at ≪10-cm length scales (*18*). Overall subsurface layering structure appears to generally be horizontal along rover traverses in the Máaz formation parallel to the boundary of Séitah. However, when the rover path becomes more perpendicular to the boundary of Séitah during Sols 135, 169, 170, and 178, the layering structure appears to dip downward away from Séitah at angles of up to 15° (see highlighted regions A to D in Figs. 1 and 2). The configuration of these downward dipping layers away from Séitah's eastern and southern boundaries shows that the Séitah formation lies stratigraphically below the members of Máaz formation sampled by the rover (*19*).

[1]University of Oslo, Kjeller and Oslo, Norway. [2]University of California, Los Angeles, Los Angeles, CA, USA. [3]Jet Propulsion Laboratory, California Institute of Technology, Pasadena, CA, USA. [4]Vestfonna Geophysical, Trondheim, Norway. [5]University of Arizona, Tucson, AZ, USA. [6]Centro de Astrobiología (CSIC-INTA), Madrid, Spain. [7]Cornell University, Ithaca, NY, USA. [8]Planetary Science Institute, Tucson, AZ, USA. [9]Norwegian Polar Institute, Tromsø, Norway. [10]Technische Universität Dresden, Dresden, Germany.
*Corresponding author. Email: s.e.hamran@its.uio.no

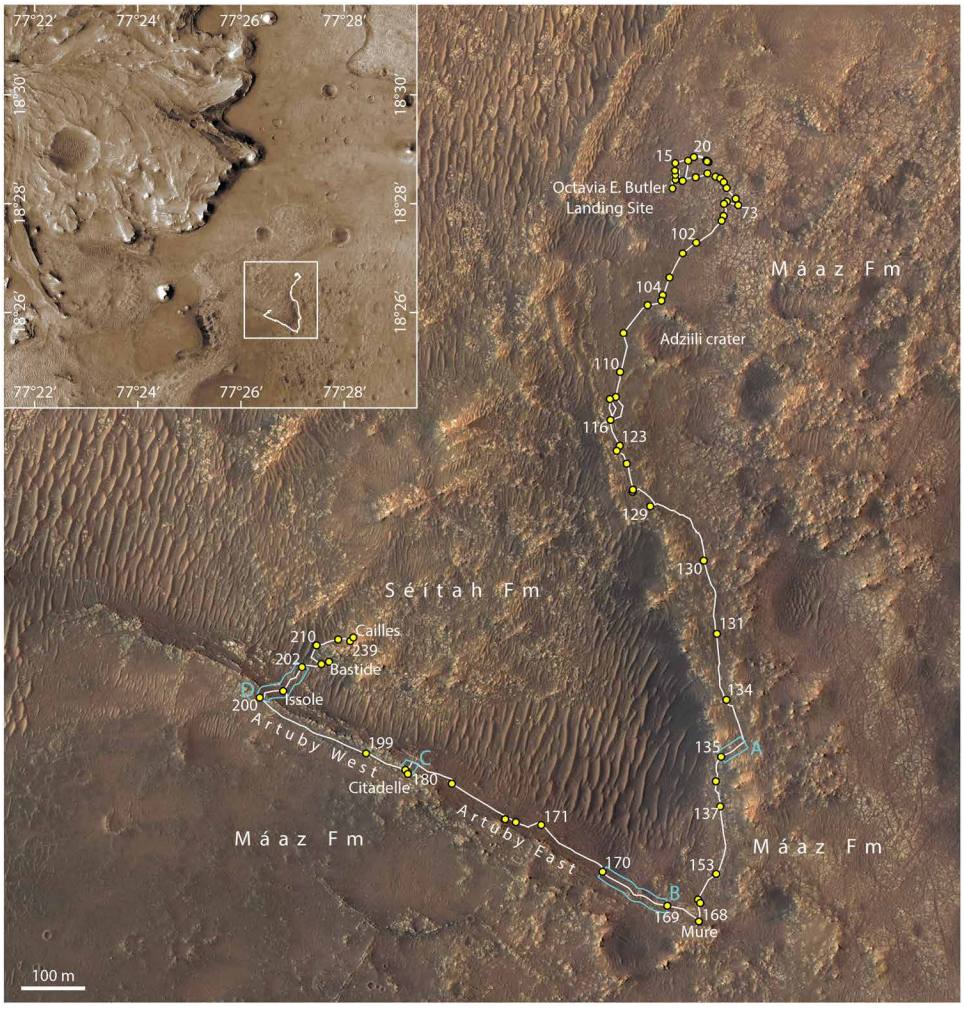

Fig. 1. High Resolution Imaging Science Experiment (HiRISE) orbital color image map of the Perseverance rover sol path from Sol 0 to Sol 204. The white numbers indicate the rover's sol traverse end points. Traverse path segments A to D highlight sections (blue boxes) where the rover traverse path was generally perpendicular to the boundary of Séítah and dipping reflectors are observed (see Fig. 2). HIRISE images ESP_037330_1990, ESP_037396_1985, ESP_037818_1990, ESP_042315_1985, ESP_045994_1985, ESP_046060_1985, ESP_048842_1985, and ESP_048908_1985 are used in this map.

During Sols 201 and 202, RIMFAX observed an 80-m-long section as the rover traversed to the north-east perpendicularly across the Artuby Ridge into Séítah that includes a range of diagnostic radar facies [see Fig. 4 (A and B) and fig. S4]. Most notable are strongly reflecting, dipping reflectors extending from the surface to depths of ~15 m. They are correlated with erosionally resistant rocky outcrops at the surface (Fig. 4, A and B) that run parallel to Artuby Ridge. The dipping layers represented by these strong subsurface reflectors and surface ridges are the outermost units of the Séítah formation. RIMFAX observed lower reflectivity zones between the strong reflecting layers that are correlated with bands of dusty regolith deposits at the surface. On the basis of migrated radargrams (see Materials and Methods), the apparent dip angle of the strong reflectors is 11° from horizontal along the rover path, which runs roughly 45° relative to Artuby ridge. If the layers are assumed to dip perpendicularly away from the ridge, then the true dip angle of these layers would be 15° from horizontal (see Materials and Methods and fig. S2). Vertical layer spacing varies from on the order of a few meters down to around 10 cm, which is the minimum that can be resolved by the instrument (*11*). At depths of ~10 m below the surface, the lowermost strongly reflecting layers appear to gradually become more horizontal (Figs. 4 and 5). The radar image acquired along the Brac-Issole traverse (Fig. 3) shows an absence of distinct layering structure to the east of the strong dipping reflectors associated with the Artuby Ridge. Further to the east, a strongly reflecting boundary runs at depths of ~2 to 3 m below the surface from the traverse midpoint to Brac.

DISCUSSION

Before the Perseverance landing, the units that comprise the Jezero crater floor had been interpreted to include lava flows (*20*, *21*), magmatic intrusions (*22*), impact condensates (*23*, *24*), tephra deposits (*25*–*27*), and/or aeolian (*28*) and fluvial deposits (*2*). Interpretations of in situ Perseverance rover measurements on a rock abrasion patch at Brac show that it has coarsely crystalline olivine cumulate lithology that is more likely of primary igneous rather than clastic origin (*19*). The high average subsurface permittivity determined by

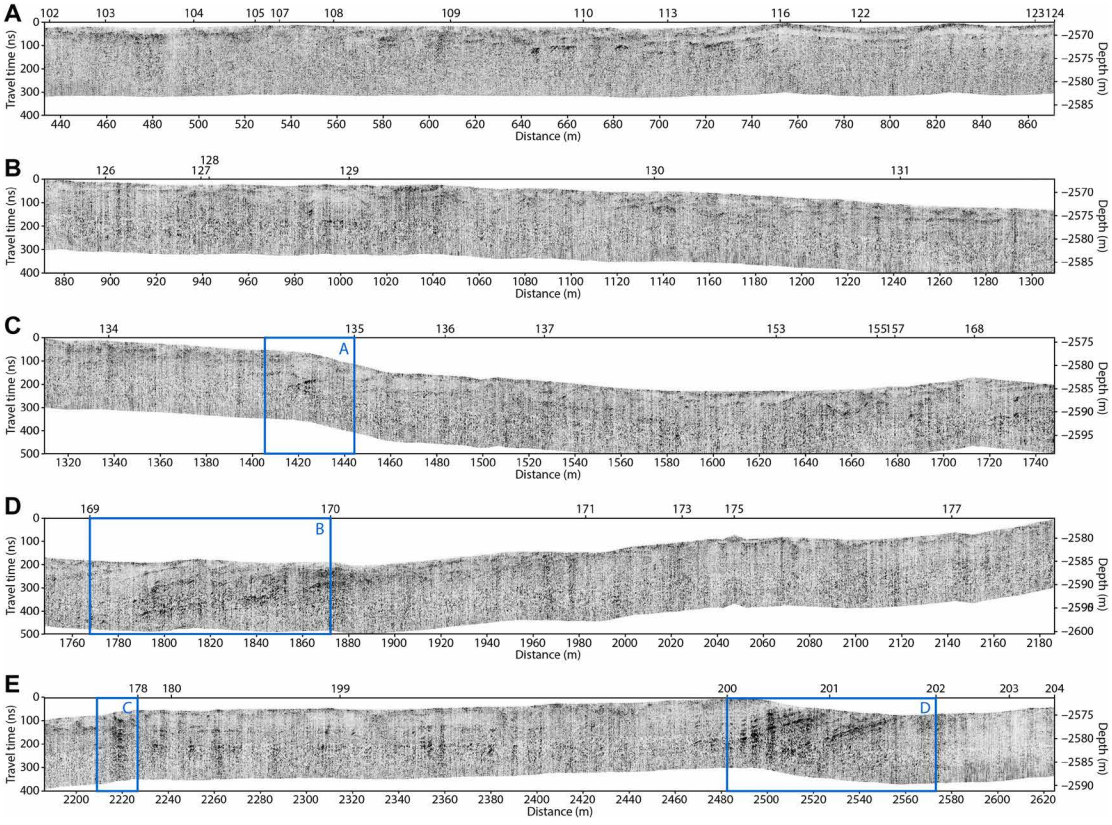

Fig. 2. RIMFAX ground-penetrating amplitude only radar image displayed at low resolution for all sounding data acquired from Sol 102 to Sol 204. Rover sol end points are shown across the top of the image. Plotted are reflected strength as a function of linear distance (in meters) and depth (in meters) with 3× vertical exaggeration, accounting for the topographic profile of the rover's traverse. Radar image in (**A**) is traverse path from Sol 102 to Sol 124, (**B**) Sol 126 to Sol 131, (**C**) Sol 134 to Sol 168, (**D**) Sol 169 to 177, and (**E**) Sol 178 to Sol 204. Traverse path segments A to D highlight sections where the rover traverse path was generally perpendicular to the boundary of Séitah and dipping reflectors are observed (see Fig. 1).

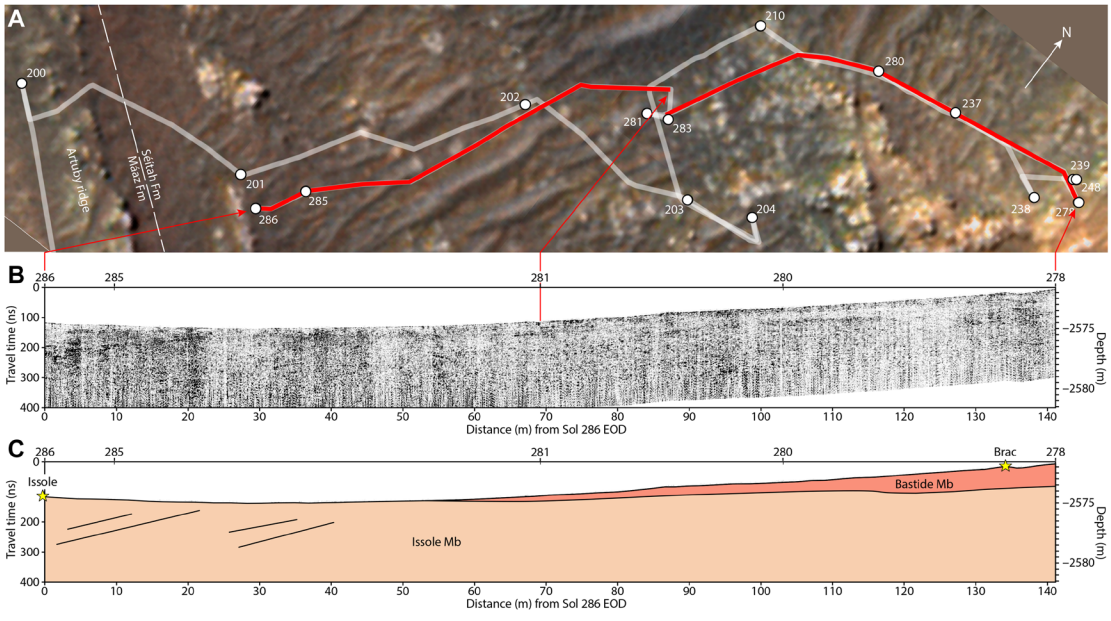

Fig. 3. RIMFAX radargram acquired from Sol 278 to Sol 286. (**A**) HiRISE orbital color image map of the Perseverance rover sol paths across Séitah between Issole and Brac. (**B**) RIMFAX reflected strength as a function of linear from distance (in meters) and depth (in meters) with no vertical exaggeration accounting for the topographic profile of the rover's traverse from Sol 278 to Sol 286 between Brac and Issole. (**C**) Interpretive cross section of the Brac-Issole traverse radar image. White lines show the rover's eastward traverse path (Sols 201 to 248). Red lines show the rover's westward traverse path (Sols 278 to 286). EOD, End of Drive.

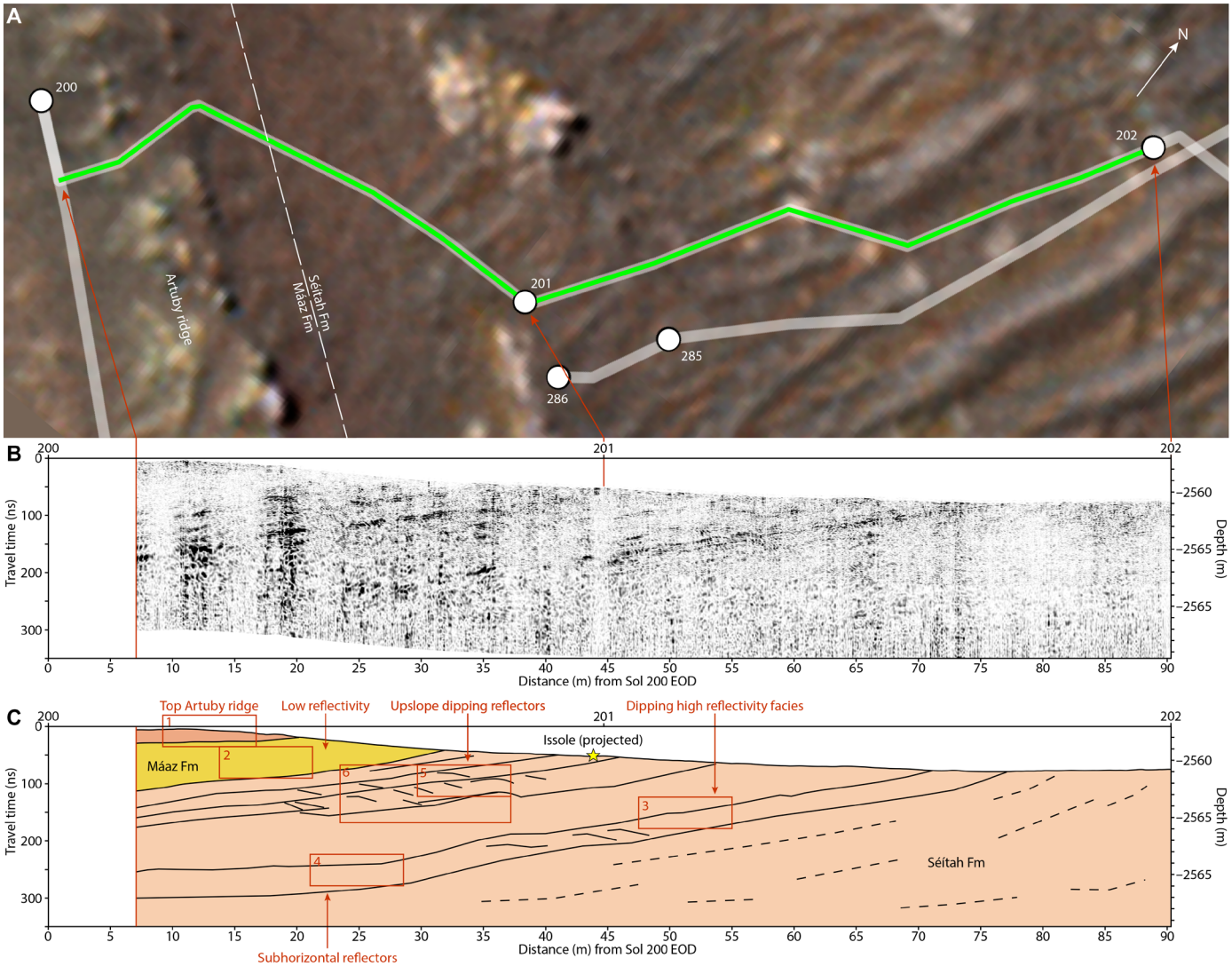

Fig. 4. RIMFAX radargram acquired from Sol 201 and Sol 202. (**A**) Sol 201 to 202 rover path from HiRISE. (**B**) RIMFAX amplitude-only radargram displayed at moderate resolution and (**C**) interpretive cross section. We have identified six selected areas (numbered 1 to 6) to illustrate high-resolution radar facies that are characteristic of the RIMFAX preconjunction dataset as a whole (Fig. 5). The larger box 6 indicates where the data shown in fig. S3B are taken.

RIMFAX is consistent with the presence of dense, low-porosity igneous rocks. The subsurface stratigraphy observed by RIMFAX is also potentially consistent with this interpretation, as igneous units on Earth can display both horizontal and inclined layered structures (*29*, *30*). Alternatively, the RIMFAX stratigraphy is also consistent with sedimentary structures formed in-place in an aqueous environment, as the dip angles of the strongly reflecting layers are consistent with those expected for foreset and bottomset beds (*31*–*33*). Since dipping layers observed near Issole appear to be discontinuous with the horizontal layers observed near Brac, it is possible that Brac and Issole may represent two different units with differing origins.

Examination of the Sol 201 and 202 radar image at highest resolution reveals the presence of multiple lenticular reflectors with sigmoidal profiles, sandwiched between the dipping high reflectivity layers (Fig. 5 and figs. S4 and S5), that have dip angles too steep to be consistent with diffraction hyperbolas for nadir and off-nadir scatterers (see Materials and Methods and fig. S1). These finer layers have along-track wavelengths of 2 to 4 m and dip angles that are comparable to those of the high reflectivity layers but in the opposite direction. The sheer dimensions and consistency of the radar facies requires that the lenticular reflectors are connected to the large strong reflecting layers and are not an artifact of interference from off-nadir structures.

One explanation for the subsurface lenticular reflectors observed by RIMFAX is that they are igneous structures associated with the emplacement of a layered magma body (fig. S3). High-resolution ground-penetrating radars on Earth that do not penetrate as deeply into dense igneous units as RIMFAX is able to on Mars because of increased loss due to dielectric absorption and higher conductivity from water in the ground, and analogous terrestrial radar facies have not been observed in terrestrial field measurements. The RIMFAX lenticular reflectors may be interpreted as magmatic flow and shear structures as are observed in outcrops at margins of terrestrial magma bodies at similar scale (*34*).

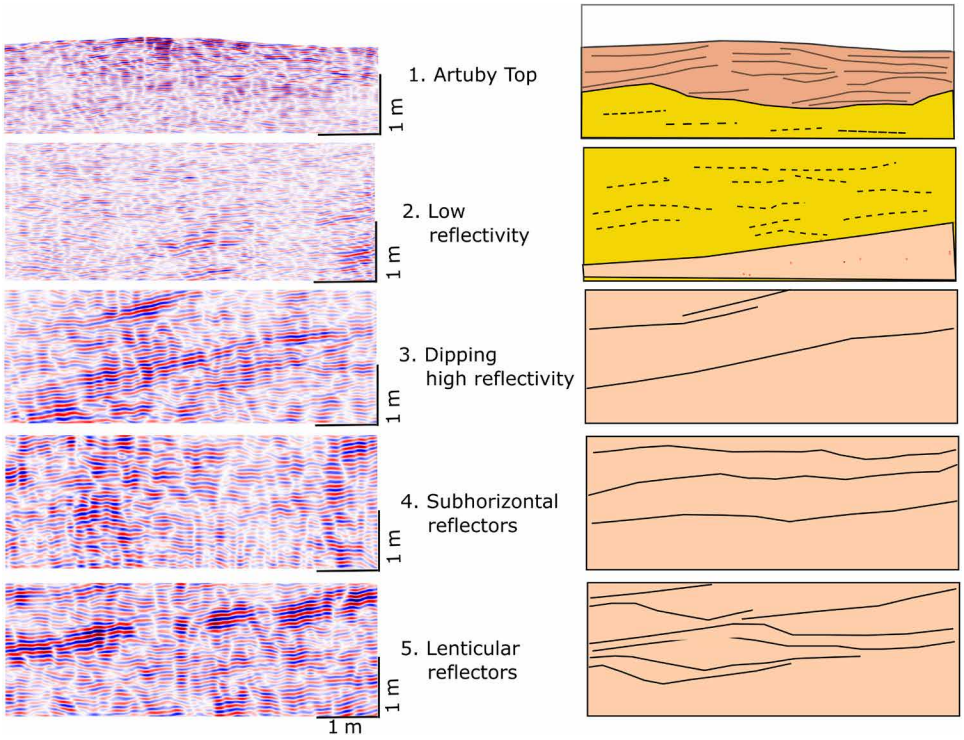

Fig. 5. RIMFAX radar facies observed during Sol 201 and Sol 202. The different radar facies are indicated by the numbered boxes in Fig. 4C displayed at high resolution (**left**) and associated interpretations (**right**). The Artuby Top Facies (Radar facies 1) exhibits coherent near-surface layering that is subparallel to the local topography to depths of ~1 m. The Low Reflectivity Facies (Radar facies 2) is a 2- to 4-m-thick subsurface zone that is relatively free of coherent scatterers that can be traced for hundreds of meters as the rover traversed parallel to Artuby Ridge during Sols 178 to 200 (Fig. 2). The Low Reflectivity Facies appears to lie conformably on top of the Dipping High Reflectivity Facies (Radar facies 3), and we interpret it to be part of the same sequence of dipping layers that outcropped on the surface during the Sol 201 to 202 traverse. The Dipping High Reflectivity Facies consists of a set of strongly reflecting dipping parallel layers that are organized into packages with thicknesses that vary from 1 to 6 m. At ~10-m depth, the Dipping High Reflectivity Facies gradually become less highly inclined to form Deep Sub-Horizontal Facies (Radar facies 4). Last, there are also Upslope Dipping Facies (Radar facies 5) consisting of multiple lenticular reflectors with sigmoidal profiles sandwiched between the Dipping High Reflectivity layers with horizontal scales of 2 to 4 m (see fig. S3).

Alternatively, the lenticular reflectors may be cyclic step structures that are commonly observed in sedimentary environments on Earth (*35*–*40*) and on Mars (*41*, *42*). Cyclic steps of similar scale and morphology have been identified in 200-MHz to 1.5-GHz ground-penetrating radar surveys of terrestrial glacigenic subaqueous fan and delta settings and correlated sedimentary facies visible in outcrops (fig. S4) (*43*). Cyclic steps can be differentiated from related cross-bedded clinoform structures. Subaqueous dunes, which form in subcritical flow regimes, have downslope-migrating lee-side depositional bedding patterns, which are opposite to those that we observe (fig. S6) (*36*). Subaqueous antidunes form in supercritical flow regimes and have symmetrical undulations rather than the strongly reflecting set boundary structures that we observe (*36*). Aeolian dunes also have lee-side depositional bedding patterns and have slopes of 29° to 34° on Mars (*44*), which are higher than what we observe. The weaker-reflecting backstepping layers and the stronger-reflecting set-boundary reflectors observed during Sols 201 and 202 have approximately equal dip angles, which would imply formation in a mixed partially depositional, partially erosional environment (*36*).

The discovery of buried structures in the Jezero crater floor is potentially compatible with a history of long-lived igneous activity and a history of multiple aqueous episodes. Interpretations of available Perseverance rover in situ characterizations of surface outcrops favor an igneous origin. However, the high-resolution radar facies associated with the steeply dipping layers of the Artuby ridge observed by RIMFAX strongly resemble those associated with aqueous sedimentary deposits. In either case, the initial RIMFAX data demonstrate the great potential of ground-penetrating radar surveys to reveal subsurface geologic structures on Mars.

MATERIALS AND METHODS

Planetary Data System dataset and processing

The data used in this work can be found in the NASA PDS Geosciences Node (*12*). The processing of the data is the same as described in the RIMFAX Calibrated Data Record Software Interface Specification. A gain with depth has been applied to the time domain data before displaying them.

The radar wave velocity in the subsurface is not well constrained, as described in the section below. This means that migrating the data sometimes increases the noise level in the resulting image. Figures 2 to 5 therefore use unmigrated data to better preserve the image details. In fig. S4, a Kirchhoff migration with a two-layer velocity is used. The velocity model has a 75-cm air layer between the antenna and the ground with a subsurface velocity of 0.1 m/ns. Figures 2 to 4 show the magnitude of the reflected

data, while the other radargrams show the real part of the waveform data.

Permittivity/wave velocity estimation

The relative dielectric permittivity ε' can be derived from the radar wave propagation velocity v, assuming a dry, nonmagnetic, low-loss material, such that $v = c/\sqrt{(\varepsilon')}$ holds, with speed of light c in free space. For the velocity derivation, we adapt the hyperbola matching method, a common technique used on Earth and for Moon-based ground-penetrating radar (*10*, *45*). The characteristic reflection pattern for line measurements over a buried subwavelength-sized diffractor such as boulders or cavities is a hyperbola. Its shape is determined by the average velocity of the overlying material; thus, matching an analytic travel time curve to the hyperbolic shape yields the velocity. Here, we account for the refraction at the Martian surface by using a two-layered model with atmosphere and homogeneous subsurface (*46*). The average permittivity along the traverse is 9.0 with an SD of 2.8 and an average diffractor depth of 1.9 m with 1.1-m SD.

SUPPLEMENTARY MATERIALS

Supplementary material for this article is available at https://science.org/doi/10.1126/sciadv.abp8564

REFERENCES AND NOTES

1. C. I. Fassett, J. W. Head III, Fluvial sedimentary deposits on Mars: Ancient deltas in a crater lake in the Nili Fossae region. *Geophys. Res. Lett.* **32**, L14201 (2005).
2. T. A. Goudge, J. F. Mustard, J. W. Head, C. I. Fassett, S. M. Wiseman, Assessing the mineralogy of the watershed and fan deposits of the Jezero crater paleolake system, Mars. *J. Geophys. Res. Planets* **120**, 775–808 (2015).
3. T. A. Goudge, D. Mohrig, B. T. Cardenas, C. M. Hughes, C. I. Fassett, Stratigraphy and paleohydrology of delta channel deposits, Jezero crater, Mars. *Icarus* **301**, 58–75 (2018).
4. B. H. N. Horgan, R. B. Anderson, G. Dromart, E. S. Amador, M. S. Rice, The mineral diversity of Jezero crater: Evidence for possible lacustrine carbonates on Mars. *Icarus* **339**, 113526 (2020).
5. A. J. Brown, C. E. Viviano, T. A. Goudge, Olivine-carbonate mineralogy of the Jezero crater region. *J. Geophys. Res. Planets* **125**, e2019JE006011 (2020).
6. K. M. Stack, N. R. Williams, F. Calef III, V. Z. Sun, K. H. Williford, K. A. Farley, S. Eide, D. Flannery, C. Hughes, S. R. Jacob, L. C. Kah, F. Meyen, A. Molina, C. Q. Nataf, M. Rice, P. Russell, E. Scheller, C. H. Seeger, W. J. Abbey, J. B. Adler, H. Amundsen, R. B. Anderson, S. M. Angel, G. Arana, J. Atkins, M. Barrington, T. Berger, R. Borden, B. Boring, A. Brown, B. L. Carrier, P. Conrad, H. Dypvik, S. A. Fagents, Z. E. Gallegos, B. Garczynski, K. Golder, F. Gomez, Y. Goreva, S. Gupta, S.-E. Hamran, T. Hicks, E. D. Hinterman, B. N. Horgan, J. Hurowitz, J. R. Johnson, J. Lasue, R. E. Kronyak, Y. Liu, J. M. Madariaga, N. Mangold, J. M. Clean, N. Miklusicak, D. Nunes, C. Rojas, K. Runyon, N. Schmitz, N. Scudder, E. Shaver, J. S. Hoo, R. Spaulding, E. Stanish, L. K. Tamppari, M. M. Tice, N. Turenne, P. A. Willis, R. A. Yingst, Photogeologic map of the perseverance rover field site in Jezero crater constructed by the Mars 2020 Science Team. *Space Sci. Rev.* **216**, 127 (2020).
7. K. H. Williford, K. A. Farley, K. M. Stack, A. C. Allwood, D. Beaty, L. W. Beegle, R. Bhartia, A. J. Brown, M. de la Torre Juarez, S.-E. Hamran, M. H. Hecht, J. A. Hurowitz, J. A. Rodriguez-Manfredi, S. Maurice, S. Milkovich, R. C. Wiens, Chapter 11 - The NASA Mars 2020 rover mission and the search for extraterrestrial life, in *From Habitability to Life on Mars*, N. A. Cabrol, E. A. Grin, Eds. (Elsevier, 2018), pp. 275–308.
8. K. A. Farley, K. H. Williford, K. M. Stack, R. Bhartia, A. Chen, M. de la Torre, K. Hand, Y. Goreva, C. D. K. Herd, R. Hueso, Y. Liu, J. N. Maki, G. Martinez, R. C. Moeller, A. Nelessen, C. E. Newman, D. Nunes, A. Ponce, N. Spanovich, P. A. Willis, L. W. Beegle, J. F. Bell III, A. J. Brown, S.-E. Hamran, J. A. Hurowitz, S. Maurice, D. A. Paige, J. A. Rodriguez-Manfredi, M. Schulte, R. C. Wiens, Mars 2020 mission overview. *Space Sci. Rev.* **216**, 142 (2020).
9. D. J. Daniels, *Ground Penetrating Radar* (IEEE, ed. 2, 2004).
10. H. M. Jol, *Ground Penetrating Radar Theory and Applications* (Elsevier, 2008).
11. S. E. Hamran, D. A. Paige, H. E. F. Amundsen, T. Berger, S. Brovoll, L. Carter, L. Damsgård, H. Dypvik, J. Eide, S. Eide, R. Ghent, Ø. Helleren, J. Kohler, M. Mellon, D. C. Nunes, D. Plettemeier, K. Rowe, P. Russell, M. J. Øyan, Radar imager for Mars' subsurface experiment—RIMFAX. *Space Sci. Rev.* **216**, 128 (2020).
12. S.-E. Hamran, D. A. Paige, Mars 2020 perseverance rover RIMFAX raw and calibrated data products (NASA PDS Geosciences Node, 2021); https://doi.org/10.17189/1522644.
13. M. J. Campbell, J. Ulrichs, Electrical properties of rocks and their significance for lunar radar observations. *J. Geophys. Res.* **74**, 5867–5881 (1969).
14. A. C. Rust, J. K. Russell, R. J. Knight, Dielectric constant as a predictor of porosity in dry volcanic rocks. *J. Volcanol. Geotherm. Res.* **91**, 79–96 (1999).
15. E. Heggy, S. M. Clifford, R. E. Grimm, C. L. Dinwiddie, D. Y. Wyrick, B. E. Hill, Ground-penetrating radar sounding in mafic lava flows: Assessing attenuation and scattering losses in Mars-analog volcanic terrains. *J. Geophys. Res.* **111**, E06S04 (2006).
16. G. R. Olhoeft, D. W. Strangway, Dielectric properties of the first 100 meters of the moon. *Earth Planet. Sci. Lett.* **24**, 394–404 (1975).
17. D. E. Stillman, G. Olhoeft, Frequency and temperature dependence in electromagnetic properties of Martian analog minerals. *J. Geophys. Res.* **113**, E09005 (2008).
18. O. Akinpelu, "Ground penetrating radar imaging of ancient clastic deposits: A tool for three-dimensional outcrop studies," thesis, University of Toronto, Canada, 2011.
19. K. A. Farley, K. M. Stack, B. H. N. Horgan, J. Tarnas, V. Z. Sun, D. L. Shuster, J. I. Simon, J. A. Hurowitz, K. R. Moore, E. L. Scheller, M. E. Schmidt, T. V. Kizovski, P. S. Russell, P. Vasconcelos, N. J. Tosca, O. Beyssac, T. Bosak, B. L. Ehlmann, L. E. Mayhew, S. M. McLennan, A. H. Treiman, R. C. Wiens, K. H. Williford, *et al.*, Aqueously altered igneous rocks on the floor of Jezero crater, Mars. *Science*, abo2196 (2022).
20. L. L. Tornabene, J. E. Moersch, H. Y. McSween Jr., V. E. Hamilton, J. L. Piatek, P. R. Christensen, Surface and crater-exposed lithologic units of the Isidis Basin as mapped by coanalysis of THEMIS and TES derived data products. *J. Geophys. Res.* **113**, E10001 (2008).
21. A. Ody, F. Poulet, J.-P. Bibring, D. Loizeau, J. Carter, B. Gondet, Y. Langevin, Global investigation of olivine on Mars: Insights into the crust and mantle. *Geophys. Res. Planets* **118**, 234–262 (2013).
22. T. M. Hoefen, R. N. Clark, J. L. Bandfield, M. D. Smith, J. C. Pearl, P. R. Christensen, Discovery of Olivine in the Nili Fossae region of Mars. *Science* **302**, 627–630 (2003).
23. A. M. Palumbo, J. W. Head, Impact cratering as a cause of climate change, surface alteration, and resurfacing during the early history of Mars. *Meteorit. Planet. Sci.* **53**, 687–725 (2018).
24. A. D. Rogers, N. H. Warner, M. P. Golombek, J. W. Head III, J. C. Cowart, Areally extensive surface bedrock exposures on Mars: Many are clastic rocks, not lavas. *Geophys. Res. Lett.* **45**, 1767–1777 (2018).
25. M. S. Bramble, J. F. Mustard, M. R. Salvatore, The geological history of Northeast Syrtis Major, Mars. *Icarus* **293**, 66–93 (2017).
26. C. H. Kremer, J. F. Mustard, M. S. Bramble, A widespread olivine-rich ash deposit on Mars. *Geology* **47**, 677–681 (2019).
27. L. Mandon, C. Quantin-Nataf, P. Thallot, N. Mangold, L. Lozac'h, G. Dromart, P. Beck, E. Dehouck, S. Breton, C. Millot, M. Volat, Refining the age, emplacement and alteration scenarios of the olivine-rich unit in the Nili Fossae region, Mars. *Icarus* **336**, 113436 (2020).
28. M. Day, T. Dorn, Wind in Jezero Crater, Mars. *J. Geophys. Res.* **46**, 3099–3107 (2019).
29. Z. Vukmanovic, M. B. Holness, K. Monks, J. C. Ø. Andersen, The Skaergaard trough layering: Sedimentation in a convecting magma chamber. *Contrib. Mineral. Petrol.* **173**, 43 (2018).
30. C. Emeleus, V. Troll, The Rum Igneous Centre, Scotland. *Mineral. Mag.* **78**, 805–839 (2014).
31. A. K. Tary, D. M. FitzGerald, T. K. Weddle, A ground penetrating radar investigation of a glacial-marine ice-contact delta, Pineo Ridge, eastern coastal Maine, in *Stratigraphic Analyses Using GPR*, Gregory S. Baker, Harry M. Jol, Eds. (Geological Society of America Special Paper, 2007), pp. 432.
32. S. Patruno, W. Helland-Hansen, Clinoforms and clinoform systems: Review and dynamic classification scheme for shorelines, subaqueous deltas, shelf edges and continental margins. *Earth Sci. Rev.* **185**, 202–233 (2018).
33. B. Gruszka, Z. Tomasz, Lacustrine deltas and subaqueous fans: Almost the same, but different—A review. *Geologos* **27**, 43–55 (2021).
34. A. R. McBirney, A. Nicolas, The Skaergaard layered series. Part II. Magmatic flow and dynamic layering. *J. Petrol.* **38**, 569–580 (1997).
35. S. Kostic, Modeling of submarine cyclic steps: Controls on their formation, migration, and architecture. *Geosphere* **7**, 294–304 (2011).
36. A. Slootman, M. J. B. Cartigny, Cyclic steps: Review and aggradation-based classification. *Earth Sci. Rev.* **201**, 102949 (2020).
37. J. Lang, D. P. Le Heron, J. H. Van den Berg, J. Winsemann, Bedforms and sedimentary structures related to supercritical flows in glacigenic settings. *Sedimentology* **68**, 1539–1579 (2021).
38. K. Ono, P. Plink-Björklund, J. T. Eggenhuisen, M. J. B. Cartigny, Froude supercritical flow processes and sedimentary structures: New insights from experiments with a wide range of grain sizes. *Sedimentology* **68**, 1328–1357 (2021).
39. A. Slootman, D. Ventra, M. Cartigny, A. Normandeau, S. Hubbard, Supercritical-flow processes and depositional products: Introduction to thematic issue. *Sedimentology* **68**, 1289–1296 (2021).
40. J. H. van den Berg, J. Lang, Sedimentary structure of inferred cyclic-step bedforms in submarine volcaniclastic slope deposits, Cuatro Calas, south-east Spain. *Sedimentology* **68**, 1439–1464 (2021).

41. I. B. Smith, J. W. Holt, A. Spiga, A. D. Howard, G. Parker, The spiral troughs of Mars as cyclic steps. *JGR: Planets* **118**, 1835–1857 (2013).
42. S. Kostic, I. B. Smith, Water on Mars: Do submarine cyclic steps exist on the red planet? *Prog Earth Planet Sci* **5**, 76 (2018).
43. J. Lang, J. Sievers, M. Loewer, J. Igel, J. Winsemann, 3D architecture of cyclic-step and antidune deposits in glacigenic subaqueous fan and delta settings: Integrating outcrop and ground-penetrating radar data. *Sedimentary Geol.* **362**, 83–100 (2017).
44. C. Atwood-Stone, A. S. McEwen, Avalanche slope angles in low-gravity environments from active Martian sand dunes. *Geophys. Res. Lett.* **40**, 2929–2934 (2013).
45. C. Li, Y. Su, E. Pettinelli, S. Xing, C. Ding, J. Liu, X. Ren, S. E. Lauro, F. Soldovieri, X. Zeng, X. Gao, W. Chen, S. Dai, D. Liu, G. Zhang, W. Zuo, W. Wen, Z. Zhang, X. Zhang, H. Zhang, The Moon's farside shallow subsurface structure unveiled by Chang'E-4 Lunar Penetrating Radar. *Sci. Adv.* **6**, aay6898 (2020).
46. T. M. Casademont, S.-E. Hamran, H. E. F. Amundsen, S. Eide, H. Dypvik, T. Berger, P. Russell, Dielectric permittivity and density of the shallow martian subsurface in Jezero crater, in *Lunar and Planetary Science Conference* (2022), pp. 1513; www.hou.usra.edu/meetings/lpsc2022/pdf/1513.pdf.
47. O. E. Sequeiros, Estimating turbidity current conditions from channel morphology: A Froude number approach. *J. Geophys. Res.* **117**, C04003 (2012).

Acknowledgments
Funding: This work was supported by the Research Council of Norway, grant no. 309835, Centre for Space Sensors and Systems (CENSSS), through their SFI Centre for Research-based Innovation program (to S.-E.H. and T.B.), and grant no. 301238 (to T.M.C. and H.D.), and PRODEX Experiment Arrangement no. 4000130734 (to S.B., L.D., and M.J.Ø.), and the University of Oslo (to S.E.), and the Jet Propulsion Laboratory, through NASA's Mars Exploration Program (to D.A.P., M.T.M., L.C., R.G., and D.C.N.) and the Mars 2020 Participating Scientist Grant 80NSSC21K0656 (to M.S.), and the European Research Council Consolidator grant no. 818602 (to A.G.F.). Part of the research was carried out at the Jet Propulsion Laboratory, California Institute of Technology, under a contract with the National Aeronautics and Space Administration (80NM0018D0004). The development of the RIMFAX instrument was supported by The Norwegian Space Agency and The Norwegian Defence Research Establishment (FFI). **Author contributions:** S.-E.H., D.A.P., A.A., A.G.F., T.B., and T.M.C. wrote the paper. S.-E.H., H.E.F.A., S.E., and T.M.C. drew the figures. S.-E.H., T.B., T.M.C., S.E., L.D., S.B., and M.J.Ø. processed the data. S.-E.H., D.A.P., A.A., H.E.F.A., L.C., T.M.C., H.D., A.G.F., R.G., J.K., M.T.M., D.C.N., D.P., and P.R. interpreted the data. T.B., T.M.C., S.E., L.D., S.B., M.J.Ø., and P.R. planned observations. T.B., S.B., L.D., P.R., S.E., and T.M.C. planned operations. All authors reviewed the manuscript. **Competing interests:** The authors declare that they have no competing interests. **Data and materials availability:** The data used in this work are available at the NASA PDS Geosciences Node (https://doi.org/10.17189/1522644) (*12*). All data needed to evaluate the conclusions in the paper are present in the paper and/or the Supplementary Materials.

Submitted 2 March 2022
Accepted 24 May 2022
Published 25 August 2022
10.1126/sciadv.abp8564